# Retrieving Land Surface Temperature From Chinese FY-3D MERSI-2 Data Using an Operational Split Window Algorithm

Kai Tang 🆔, Hongchun Zhu 🆔, Ping Ni, Ruibo Li, and Cheng Fan

*Abstract*—Medium resolution spectral imager II (MERSI-2) is a payload for the Chinese meteorological satellite Feng Yun 3 (FY-3). China's satellite remote sensing observation capabilities such as climate change research can be improved during MERSI-2's operation in orbit, and the sensor is the world's first imaging instrument that can obtain a global infrared split-window data with a spatial resolution of 250 m. We developed an operational spilt-window (SW) algorithm to retrieve land surface temperature (LST) accurately from the MERSI-2 data. The SW algorithm coefficients were derived from a simulation dataset that was established with the Moderate spectral resolution atmospheric Transmittance model version 5.2 and the thermodynamic initial guess retrieval dataset. In the practical retrieval, the precise algorithm coefficients were determined by view zenith angle and atmospheric water vapor content (WVC), the atmospheric WVC were obtained from the ERA5 dataset, and the land surface emissivity was dynamically estimated using the advanced spaceborne thermal emission and reflection radiometer global emissivity dataset, considering the fractional of vegetation cover and snow cover. The retrieved LST compared with *in situ* LST, which was highly consistent with the *in situ* LST and that the root-mean-square error of the two is within 3 K. The retrieved LST was compared with the MYD11_L2 and MYD21_L2 LST products, and the results indicated that MERSI-2 LST was more consistent with the MYD21 LST. The operational SW algorithm for FY-3D MERSI-2 developed in this study could retrieve LST accurately and has a wide range of popularization and application values.

*Index Terms*—Feng Yun (FY)-3D medium resolution spectral imager II (MERSI-2), land surface emissivity (LSE), land surface temperature (LST), operational split-window (SW) algorithm, validation.

Kai Tang, Hongchun Zhu, and Ping Ni are with the School of College of Geodesy and Geomatics, Shandong University of Science and Technology, Qingdao 266590, China (e-mail: tangkai_sdust@foxmail.com; sdny_xa@163.com; niping_sdust@163.com).

Ruibo Li is with the School of College of Geodesy and Geomatics, Shandong University of Science and Technology, Qingdao 266590, China, and also with the State Key Laboratory of Remote Sensing Science, Aerospace Information Research Institute, Chinese Academy of Sciences, Beijing 100101, China (e-mail: lrb0106@sdust.edu.cn).

Cheng Fan is with the State Environment Protection Key Laboratory of Satellite Remote Sensing, Aerospace Information Research Institute, Chinese Academy of Sciences, Beijing 100101, China, and also with the School of University of Chinese Academy of Sciences, Beijing 100049, China (e-mail: fancheng@radi.ac.cn).

## I. INTRODUCTION

LAND surface temperature (LST) is one of the key parameters in land surface physical process on regional and global scales, and accurate LST is essential for the study, such as climate, hydrology, and ecology [1]–[4]. Traditionally, the ground measurements cannot practically achieve an aim that measures the LST over wide and continuous areas. With the development of remote sensing from space, satellite remote sensing offers the only possibility for measuring LST over the entire globe with a sufficiently high-temporal resolution and with a large continuous area [5].

In the past 40 years, LST was retrieved using thermal infrared (TIR) data and has been significantly developed. A large number of LST retrieval algorithms have been proposed. Several typical algorithms, such as the split-window (SW) algorithm [6]–[9], single-channel algorithm [10], [11], and temperature and emissivity separation (TES) algorithm [12]–[14]. SW algorithm could estimate LST based on differential water vapor absorption in two adjacent TIR bands, which do not need to eliminate the influence of atmosphere using some information about real-time atmospheric profiles. Therefore, the SW algorithm is practical and efficient [15], [16]. The SW algorithm has been currently applied to several satellites sensors, such as MODIS [17], ASTER [18], VIRR [19]–[21], Landsat series [22]–[25], VIIRS [26], SLTSR [27], and GaoFen-5 [28]–[30]. Land surface emissivity (LSE) is an important parameter of the SW algorithm, in which the uncertainty of 0.01 in LSE can lead to LST error of approximately 0.60 K [31]–[33]. A variety of methods have been proposed to estimate LSE input into the SW algorithm, including classification-based emissivity method [34], normalized difference vegetation (NDVI) index-based threshold method [35], [36], and vegetation cover method [37]. Soil emissivity varies greatly in the TIR bands [38]. However, these methods cannot well characterize the emissivity variation over the bare soil surface in arid and semiarid lands [39], [40]. For example, several studies have indicated that the Collection 5 MODIS LST product using classification-based emissivity method overestimates bare soil emissivity leads to the serious underestimation of the LST [41], [42]. The National Aeronautics and Space Administration released a new emissivity dataset named the ASTER global emissivity dataset (ASTER GED) in 2014, which is a global mean emissivity database produced using all clear-sky ASTER images from 2000 to 2008

TABLE I
MAJOR PARAMETERS OF MERSI-2 BANDS

| Band No. | Centroid wavelength (μm) | Spectral bandwidth(nm) | IFOV (m) | NE△ρ%)/△T | Dynamic Range(ρ/K) |
|---|---|---|---|---|---|
| 1 | 0.470 | 50 | 250 | 100 | 90% |
| 2 | 0.550 | 50 | 250 | 100 | 90% |
| 3 | 0.650 | 50 | 250 | 100 | 90% |
| 4 | 0.865 | 50 | 250 | 100 | 90% |
| 5 | 1.38 | 20/30 | 1000 | 60/100 | 90% |
| 6 | 1.64 | 50 | 1000 | 200 | 90% |
| 7 | 2.13 | 50 | 1000 | 100 | 90% |
| 8 | 0.412 | 20 | 1000 | 300 | 30% |
| 9 | 0.443 | 20 | 1000 | 300 | 30% |
| 10 | 0.490 | 20 | 1000 | 300 | 30% |
| 11 | 0.555 | 20 | 1000 | 500 | 30% |
| 12 | 0.670 | 20 | 1000 | 500 | 30% |
| 13 | 0.709 | 20 | 1000 | 500 | 30% |
| 14 | 0.746 | 20 | 1000 | 500 | 30% |
| 15 | 0.865 | 20 | 1000 | 500 | 30% |
| 16 | 0.905 | 20 | 1000 | 200 | 100% |
| 17 | 0.936 | 20 | 1000 | 100 | 100% |
| 18 | 0.940 | 50 | 1000 | 200 | 100% |
| 19 | 1.03 | 20 | 1000 | 100 | 100% |
| 20 | 3.8 | 180 | 1000 | 0.25 K | 200–350 K |
| 21 | 4.050 | 155 | 1000 | 0.25 K | 200–380 K |
| 22 | 7.2 | 500 | 1000 | 0.30 K | 180–280 K |
| 23 | 8.550 | 300 | 1000 | 0.25 K | 180–300 K |
| 24 | 10.8 | 1000 | 250 | 0.40 K | 180–330 K |
| 25 | 12.0 | 1000 | 250 | 0.40 K | 180–330 K |

TABLE II
SUMMARY OF THE INPUTS USED IN LST RETRIEVAL USING THE OPERATIONAL SW ALGORITHM

| Data | Temporal Resolution | Spatial Resolution | Purpose |
|---|---|---|---|
| FY-3 MERSI-2 | 5.5 days | 250 m | brightness temperature, FVC of daytime, angle information, geolocation |
| ERA5 atmospheric reanalysis | 1 h | 0.25° | water vapor content |
| ASTER GEDv3 | multi-year average (2000 to 2008) | 100 m | bare soil component emissivity per pixels |
| MYD13Q1 | 16 days | 250 m | FVC of nighttime |
| MYD10A1 | daily | 500 m | snow fraction |

[43]. Several validations have shown that this emissivity product has high accuracy over bare soil surface in arid and semiarid lands [44], [45]. Therefore, to characterize the variation of bare soil emissivity relatively accurately, this dataset has been used in emissivity estimation for many satellites sensors [46]–[49].

Feng Yun 3 (FY-3) is a second-generation polar-orbiting satellite in the Chinese meteorological satellite series, Fengyun (FY). The FY-3D satellite was launched in November 2017 with a mounted medium resolution spectral imager II (MERSI-2), a payload that is a major upgrade from the first generation homo-orbital sensor MERSI-1 [50]. MERSI-2 is the world's first imaging instrument that can obtain a global infrared SW data with a spatial resolution of 250 m [51]. MERSI-2 has a great potential in LST retrieval by its advantage of the spatial resolution in two TIR bands (band 24: 10.30–11.30 μm and band 25: 11.50–12.50 μm). Several studies have been currently carried out based on the MERSI-2 data about the atmospheric and land surface parameters, such as aerosol [52], water vapor, and soil moisture [53]. However, the study of MERSI-2 about LST retrieval is rare. Wang *et al.* [51] developed an SW algorithm for MERSI-2 through a linear simplified plank function. The mean-absolute errors of Wang's SW algorithm are 0.42, 1.37, and 1.23 K when compared with simulation data, MODIS LST (MYD11A1), and ground measurements, respectively. This algorithm needs some input parameters, such as atmospheric transmittance and LSE, which were calculated from the near-infrared bands and red band. Therefore, all the needed parameters of the algorithm can be obtained from the sensing images of the same sensor, but the real-time atmospheric transmittance cannot be obtained when the data are imaging at night, and the algorithm did not consider the effect of a sensor observation angle. Jiang *et al.* [54] established a simulation database using moderate

spectral resolution atmospheric transmittance model version 5.2 (MODTRAN 5.2) and thermodynamic initial guess retrieval (TIGR) dataset, obtained the coefficients of generalized SW (GSW) of MERSI-2, and verified the accuracy of the algorithm using MODTRAN built-in profiles. The root-mean-square error (RMSE) of the GSW algorithm is 0.5 K when viewing zenith angles (VZA) is less than 30°, which uses a simulation database. Nevertheless, Jiang *et al.* did not further study the needed parameters of algorithm such as atmospheric water vapor content (WVC), LSE, and lacked validation through *in situ* measurements and other satellite LST products.

The objective of this study is to develop an operational SW algorithm to retrieve LST accurately from MERSI-2 data. In particular, the ASTER GED and fractional of vegetation cover (FVC) were used together to estimate accurate and dynamic LSE to enhance the accuracy of retrieved LST. An evaluation of the accuracy of the LST retrieval algorithm in practice is crucial [55], [56]. Therefore, two different methods were used to validate the retrieved LST of MERSI-2, namely, validating through *in situ* LST and comparing with MERSI-2 LST and MODIS LST products.

## II. DATA

### A. FY-3D MERSI-2 Data

FY-3D is the fourth satellite in China's second-generation polar-orbiting meteorological satellite family, which was launched in November 2017. MERSI-2 is a payload for FY-3D. The main task of MERSI-2 is to monitor dynamically the Earth's oceans, land, atmosphere, and other environmental parameters, such as cloud characteristics, aerosols, land surface characteristics, ocean surface characteristics, and low-level water vapor. China's satellite remote sensing observation capabilities in weather forecasting, climate change research, and global environmental monitoring can be improved during MERSI-2's operation in orbit. MERSI-2 has 25 bands (as shown in Table I) with a scanning range of ±55.4° and a sensor spectral coverage of 0.412–12.0 μm. The 25 bands included 10 visible bands (0.402–0.756 μm), six near-infrared bands (0.815–1.04 μm), three shortwave-infrared bands (1.37/1.365–2.155 μm), two medium-wave infrared bands (3.71–4.1275 μm), and four long-wave infrared bands (6.95–12.5 μm). In terms of band

TABLE III
MEAN VALUES OF LST STDEV WITHIN 270 × 270 M AND THE BASIC INFORMATION OF SURFRAD SITES

| Site | Name | Latitude | Longitude | Land Cover | Mean STDEV (K) | Images Number |
|------|------|----------|-----------|------------|----------------|---------------|
| DRA | Desert Rock | 36.6232 | -116.0196 | arid shrubland | 0.35 | 14 |
| GWN | Goodwin Creek | 34.2547 | -89.8729 | grassland | 0.31 | 3 |
| TBL | Table Mountain | 40.1256 | -105.2378 | sparse grassland | 0.45 | 14 |
| PSU | Penn State | 40.7201 | -77.9309 | cropland | 0.46 | 4 |
| SXF | Sioux Falls | 43.7343 | -96.6233 | grassland | 0.37 | 14 |
| FPK | Fort Peck | 48.3079 | -105.1018 | grassland | 0.26 | 10 |
| BND | Bondville | 40.0519 | -88.3731 | cropland | 0.27 | 8 |

TABLE IV
LST RMSEs CAUSED BY USING INCORRECT COEFFICIENTS IN ADJACENT SUBRANGES

| WVC (g/cm²) | LST RMSE(K) | | | | | |
|-------------|-------------|-----------|-----------|-----------|-----------|-----------|
| | 0.0 – 1.5 | 1.0 – 2.5 | 2.0 – 3.5 | 3.0 – 4.5 | 4.0 – 5.5 | 5.0 – 6.5 |
| 0.0 – 1.5 | 0.37 | 1.50 | | | | |
| 1.0 – 2.5 | 0.80 | 0.54 | 1.60 | | | |
| 2.0 – 3.5 | | 1.31 | 0.80 | 2.26 | | |
| 3.0 – 4.5 | | | 1.72 | 0.81 | 1.39 | |
| 4.0 – 5.5 | | | | 1.38 | 0.86 | 2.31 |
| 5.0 – 6.5 | | | | | 1.92 | 0.97 |

TABLE V
RELATIVE ACCURACY OF MERSI-2 LST AND MODIS LST PRODUCTS IN BARREN AND VEGETATED AREAS

| Conditions | MYD11_L2 | | MYD21_L2 | |
|------------|----------|---------|----------|---------|
| | Bias(K) | RMSE(K) | Bias(K) | RMSE(K) |
| NDVI Lt 0.2 | 2.845 | 3.283 | 1.270 | 2.244 |
| NDVI Ge 0.2 | 2.910 | 3.299 | 1.633 | 2.285 |

application, bands 1–7 are mainly used for land and cloud boundaries; bands 8–15 are used for ocean color, plankton, and biogeochemical remote sensing; bands 16, 17, 18, 22, and 23 are used for atmospheric water vapor remote sensing; channel 19 is a cloud band; and bands 20, 21, 24, and 25 are used for land, water, and cloud temperature sensing. In this study, band 3 (0.625–0.675 $\mu$m) and band 4 (0.840–0.890 $\mu$m) data that perform imaging during daytime were used to calculate NDVI and further calculate FVC, band 24 (10.30–11.30 $\mu$m) and band 25 (11.50–12.50 $\mu$m) data were used to calculate brightness temperature, and the spatial resolution of all the used bands is 250 m.

In the phase of validation using *in situ* LST, the MERSI-2 L1 level data in 2019 and 2020 (January, February, April, May, July, August, October, and November) correspond to winter, spring, summer, autumn, and spring over the United States, which were used to retrieve LST. The cloud mask product and the means of visual interpretation were applied to identify clear pixels. In the phase of comparing the MERSI-2 LST and MODIS LST products, a MERSI-2 L1 level image was used, wherein imaging time is 04:45 (UTC) on April 3, 2019 and the location is in the range of 33°42′ to 55°49′N and 98°17′ to 140°45′E.

### B. ERA5 Atmospheric Reanalysis Data

Atmospheric parameters are usually obtained from remote sensing retrievals or the output of reanalysis products. Several studies have shown that different atmospheric reanalysis products have similar accuracy for LST retrieval [57]–[59].

Furthermore, reanalysis products could provide global atmospheric information with high-temporal resolution than satellite retrievals and may be more suitable for LST retrieval [48].

ERA5 is the latest version of the European Center for Medium-range Weather Forecasts global climate atmospheric reanalysis data released in 2018, which provides long-term historical data (from 1979 to the present). The spatial resolution of the dataset improved from 0.75° × 0.75° to 0.25° × 0.25°, and temporal resolution improved from 6 to 1 h. ERA5 has pressure-level and single-level data. In this study, the total column water vapor recorded in single-level data was used for obtaining WVC in LST retrieval.

### C. ASTER GED Data

ASTER GED provides emissivity data on a global scale. This product was produced using all ASTER data from 2000 to 2008 by the TES methods in conjunction with a water vapor scaling (WVS) atmospheric correction method [60], [61]. It was distributed as 1.0° × 1.0° tiles with the spatial resolution of 100 m and 1 km. The dataset includes the mean emissivity and standard deviation (stdev) of surface emissivity in the five TIR bands and other datasets, such as latitude, longitude, land–water mask, mean NDVI, and stdev. Several studies have shown that the ASTER GED product's mean emissivity bias in all TIR bands is approximately 0.016 [44], [62]. In this study, the ASTER GEDv3 with a spatial resolution of 100 m was used to estimate LSE for LST retrieval.

### D. MODIS Products

MYD13Q1 is a MODIS NDVI product with a spatial resolution of 250 m. The product was produced using the 16-day maximum synthesis algorithm, which can avoid cloud pollution and reduce the BRDF effect. It can be assumed that no significant change is observed in FVC every 16 days. In this study, this product was used to calculate FVC and further combined with ASTER GEDv3 to estimate the LSE dynamically when the imaging time of MERSI-2 data is nighttime.

MYD10A1 is a MODIS snow cover land product with a spatial resolution of 500 m and daily temporal resolution. The dataset set consists of a single best observation of the day for each grid selected from the MODIS/Aqua Snow Cover 5-Min L2 Swath 500 m (MYD10_L2), which was produced by adopting the normalized differential snow index. In this study, the product was used to consider changes of snow fraction in snow cover areas, such as high latitude, high-altitude areas, permanent snow/ice areas, and areas in winter.
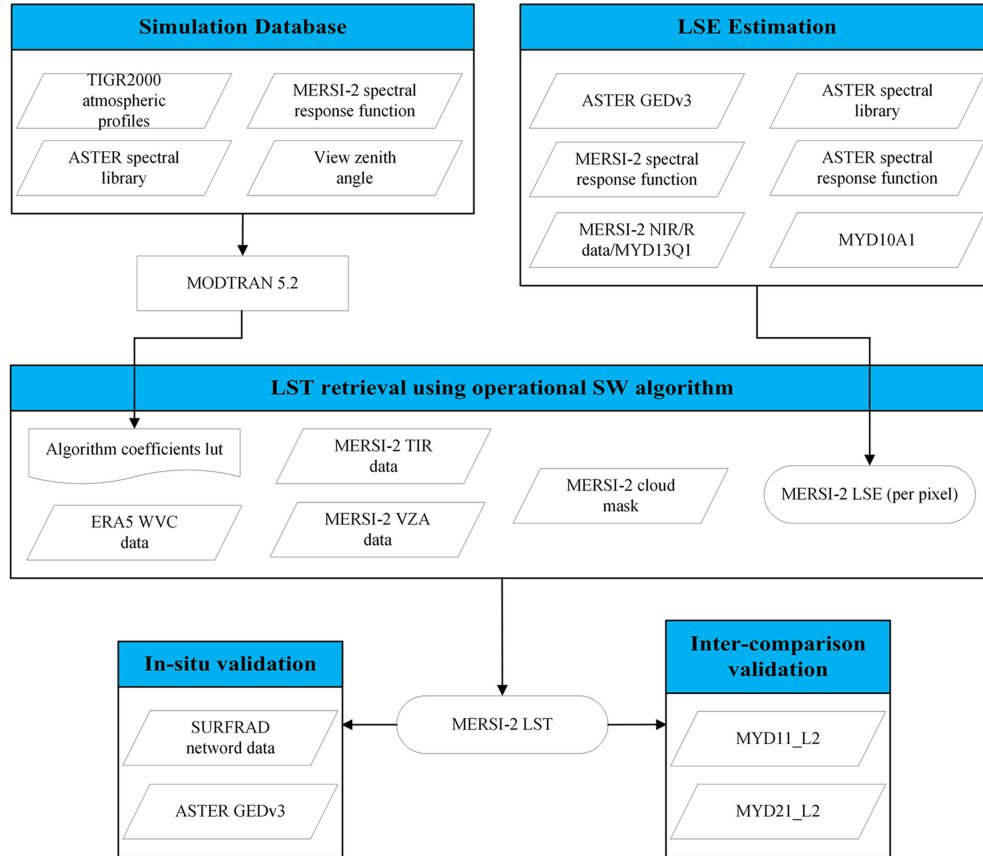
Fig. 1. Framework and technical methods.

MODIS LST products are one of the most mature LST products and have been evaluated in many previous studies [40], [41], [63]–[65]. Therefore, MODIS LST products, such as Collection 6 MYD11_L2 and Collection 6 MYD21_L2, were adopted for comparing with the retrieved LST of MERSI-2. The MYD11_L2 and MYD21_L2 products were produced using the GSW algorithm and the TES algorithm with a spatial resolution of 1 km, respectively, and the MYD21_L2 also provides dynamic LSE in three TIR bands. An improved WVS method was adopted to perform the atmospheric correction for producing MYD21, and a fast RTM, radiative transfer for (A)TOVS (RTTOV) [66], was adopted to promote the retrieval efficiency. Compared with the MYD11_L2 product, the MYD21_L2 product is more accurate over arid and semiarid lands. In this study, MYD11 L2 and MYD21 L2 products were used, in which imaging time is 04:50 (UTC) on April 3, 2019 and the location is in the range of 33°09′ to 54°45′N and 103°06′ to 138°28′E. Table II summarizes the data used in the operational SW algorithm and the corresponding information.

## III. LST RETRIEVAL AND VALIDATION METHODS FOR FY-3D MERSI-2

The framework and technical methods of this study are described in Fig. 1. The development of MERSI-2 operational SW algorithm is presented in Section III-A. The estimation of LSE is presented in Section III-B. The validation through using *in*

*situ* LST is presented in Section III-C1. The validation through comparing with MODIS LST product is presented in Section III-C2.

### A. SW Algorithm Development for FY-3D MERSI-2 Data

Based on the radiative transfer theory for a cloud-free atmosphere in thermodynamic equilibrium, the radiance is measured at the top of atmosphere (TOA) in the TIR bands as [67]:

$$B_i(T_i) = \varepsilon_i B_i(T_s)\tau_i + R^{\uparrow}_{\text{atm}\_i} + (1 - \varepsilon_i)R^{\downarrow}_{\text{atm}\_i}\tau_i \quad (1)$$

where $T_i$ is the brightness temperature of band $i$ at the TOA, $B_i$ is the Plank function, $B_i(T_s)$ is the radiance measured when the surface is a blackbody with surface temperature $T_s$, $\varepsilon_i$ is the emissivity of band $i$, $\tau_i$ is the total atmospheric transmittance along the target to sensor path in band $i$, $R^{\uparrow}_{\text{atm}\_i}$ is the thermal path atmospheric upwelling radiance of band $i$, and $R^{\downarrow}_{\text{atm}\_i}$ is the downwelling atmospheric radiance of band $i$.

Based on differential water vapor absorption in two adjacent TIR bands, SW algorithm expresses LST as a simple linear or nonlinear combination of the TOA brightness temperature of two adjacent bands and does not need real-time atmospheric profiles [30]. Therefore, SW algorithm is widely used in LST retrieval because of the feature of practical and efficient. The GSW algorithm is one of the most representative SW algorithms [7], which has been successfully used for producing several satellite LST products. Wan [68] proposed a refined GSW algorithm for

producing the MODIS Collection 6 LST product in terms of (2) to (4)

$$\text{LST} = a_0 + \left( a_1 + a_2 \frac{1-\varepsilon}{\varepsilon} + a_3 \frac{\Delta\varepsilon}{\varepsilon^2} \right) \left( \frac{T_i + T_j}{2} \right)$$

$$+ \left( a_4 + a_5 \frac{1-\varepsilon}{\varepsilon} + a_6 \frac{\Delta\varepsilon}{\varepsilon^2} \right)$$

$$\times \left( \frac{T_i - T_j}{2} \right) + a_7 (T_i - T_j)^2 \tag{2}$$

$$\bar\varepsilon = (\varepsilon_i + \varepsilon_j)/2 \tag{3}$$

$$\Delta\varepsilon = \varepsilon_i - \varepsilon_j \tag{4}$$

where $T_i$ and $T_j$ are the brightness temperature at the TOA measured of band $i$ and $j$, respectively; $\varepsilon_i$ and $\varepsilon_j$ are the emissivity of band $i$ and $j$, respectively; $\bar\varepsilon$ is the averaged emissivity of two TIR bands; $\Delta\varepsilon$ is the emissivity difference between the two adjacent bands; and $a_k (k = 0, 1, \ldots, 7)$ is an unknown coefficient.

To obtain the unknown algorithm coefficients, the MODTRAN 5.2 was used to simulate the brightness temperature of the two TIR bands of MERSI-2 with known LST, LSE, and atmospheric information. To make our operational SW algorithm applicable to most atmospheric and land surface conditions, the simulation project was designed as follows.

First, the TIGR2000 [69], [70] dataset and the spectral response functions of MERSI-2 bands 24 and 25 were input into the MODTRAN 5.2 for simulating the atmospheric transmittance, upwelling atmospheric radiance, and downwelling atmospheric radiance in TIR bands. Given that we only considered atmospheric variation in clear-sky conditions for LST retrieval, the TIGR2000 profiles with a relative humidity greater than 90% were regarded as cloudy atmosphere then discarded [21]. After the screening, a total of 946 atmospheric profiles were obtained, in which WVC was in the range of 0.06 to 6.27 g/cm² and the air temperature at the bottom boundary was in the range of 231.25 to 314.16 K. For the atmospheric transmittance and upwelling radiance, we simulated 13 VZAs from 0° to 60° with intervals of 5°. For the downwelling radiance, 53° was selected to take the place of the hemispherical value [71]. For simulating LST, the air temperature at the bottom boundary (denoted as $T_0$) of each TIGR profile was regarded as a reference. LST used for simulation was between $T_0 - 16$ K and $T_0 + 4$ K at intervals of 4 K for cold atmospheric profiles ($T_0 \leq 280$ K), and between $T_0 - 4$ K and $T_0 + 29$ K at intervals of 3 K for warm atmospheric profiles ($T_0 > 280$ K). Emissivity spectra of 61 materials, including 3 snow, 2 water, 4 vegetation, and 52 soil, were derived from ASTER spectral library [72] and convert to channel emissivity of MERSI-2 bands 24 and 25. Range of the channel emissivity of MERSI-2 bands 24 and 25 are 0.913–0.996 and 0.913–0.991, respectively. For simulating LSE, considering most land cover types, LSE was used for simulation between 0.90 and 1.0 at intervals of 0.02, and emissivity difference was used for simulation between −0.02 and 0.02 at intervals of 0.005. Then, simulative atmospheric transmittance, upwelling atmospheric radiance, downwelling atmospheric radiance, LST, LSE, emissivity difference, were substituted into (1) and the

plank function to calculate the brightness temperature at the TOA measured in MERSI-2 bands 24 and 25. Subsequently, the algorithm coefficients in (2) were obtained using regressions with the least-squared method. LST retrieval is also significantly influenced by WVC. To improve retrieval accuracy, the WVC of all 946 TIGR profiles was divided into six subranges with an overlap of 0.5 g/cm²: [0–1.5], [1–2.5], [2–3.5], [3–4.5], [4–5.5], and [5–6.5]. Considering that WVC may not be obtained in some pixels in practical retrieval, we added a WVC range between 0 and 6.5 g/cm². Finally, a lookup table of GSW algorithm coefficients for different VZAs and WVCs was established.

In the practical retrieval, suitable WVC subranges were selected according to WVC from ERA5 data, and precise algorithm coefficients were obtained by interpolating according to VZA from MERSI-2 data. For the pixel that its WVC belongs to the overlap subranges, LST was estimated with the algorithm coefficients of adjacent subranges, and then their averaged value was considered as the final LST.

### B. LSE Estimation Method

LSE for a pixel can be simply regarded as a weighted combination of vegetation and bare soil emissivity [73] in terms of

$$\varepsilon_i = \varepsilon_{v\_i} P_v + \varepsilon_{s\_i} (1 - P_v) \tag{5}$$

where $\varepsilon_i$ is the emissivity of band $i$, $\varepsilon_{v\_i}$ and $\varepsilon_{s\_i}$ are the emissivity of vegetation and bare soil components of channel $i$, respectively, and $P_v$ is the FVC, which can be calculated from

$$P_v = \left[ \frac{\text{NDVI} - \text{NDVI}_{\min}}{\text{NDVI}_{\max} - \text{NDVI}_{\min}} \right]^2 \tag{6}$$

where $\text{NDVI}_{\min}$ and $\text{NDVI}_{\max}$ are the NDVI value of the pixels of bare soil and vegetation, respectively.

Traditionally, the emissivity values of bare soil and vegetated component of each surface type were calculated according to the spectral library data, which is accurate for the vegetation part with high- and low-contrast emissivity. However, given the diverse mineral components, soil moisture content, and surface roughness, soil emissivity may vary greatly in TIR bands. Therefore, estimating the emissivity of bare soil component of each pixel in a satellite image is needed. Following the work of Wang *et al.* [38], [74] LSE in MERSI-2 bands 24 and 25 could be estimated by the ASTER GED product and FVC. The emissivity of bare soil component could be separated from ASTER means emissivity using (7), which is a variant of (5)

$$\varepsilon_{s\_\text{ASTER}} = \frac{\varepsilon_\text{ASTER} - \varepsilon_{v\_\text{ASTER}} P_{v\_\text{ASTER}}}{1 - P_{v\_\text{ASTER}}} \tag{7}$$

where $\varepsilon_\text{ASTER}$ is the LSE of a pixel from the ASTER GED product, $\varepsilon_{s\_\text{ASTER}}$ is the emissivity of bare soil of the ASTER pixel, and $\varepsilon_{v\_\text{ASTER}}$ is the emissivity of vegetation of the ASTER pixel, which is an averaged emissivity calculated by (8) with ASTER spectral response functions and vegetation emissivity spectral data from the ASTER spectral library

$$\varepsilon = \frac{\int_{\lambda_1}^{\lambda_2} f(\lambda)\varepsilon(\lambda)d\lambda}{\int_{\lambda_1}^{\lambda_2} f(\lambda)d\lambda} \tag{8}$$
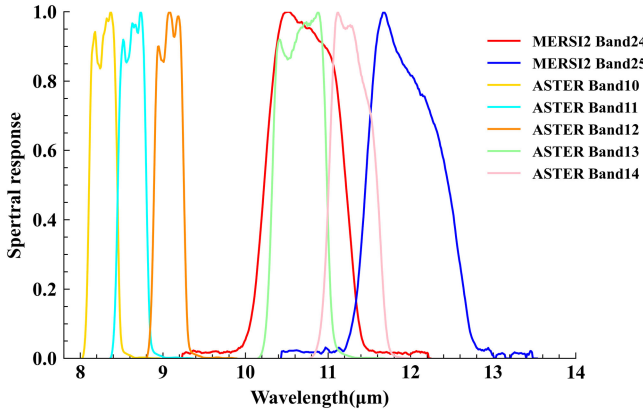
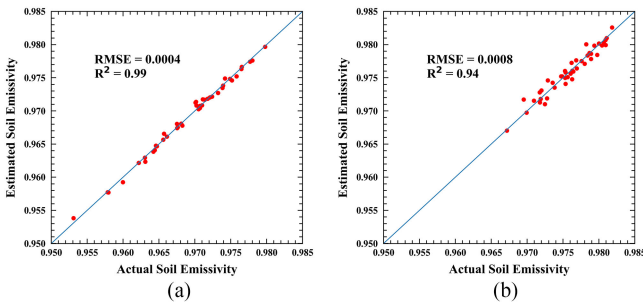Fig. 2. Spectral response functions of the MERSI-2 and ASTER TIR bands.



Fig. 3. Comparison of the estimated emissivity using (9) and (10) and the actual emissivity calculated from the ASTER spectral library at MERSI-2 bands. (a) Band 24. (b) Band 25.

where $\varepsilon(\lambda)$ is the emissivity spectral data and $f(\lambda)$ is the spectral response function of the sensor.

A spectral conversion is required between ASTER and MERSI-2 TIR bands because of the difference in band range and response (as shown in Fig. 2). As shown in (9) and (10), considering the correlation between the ASTER and MERSI-2 TIR bands, MERSI-2 band 24 emissivity was calculated using ASTER bands 13 and 14. Although MERSI-2 band 25 has little overlap with ASTER bands, it has a satisfying fitting result with ASTER bands 9–14. The coefficients in (9) and (10) were regressed from the emissivity of bare soil in MERSI-2 and ASTER TIR bands, which were calculated by (8) with bare soil emissivity spectral data from the ASTER spectral library according to the sensors spectral response function. The accuracy of (9) and (10) is shown in Fig. 3

$$\varepsilon_{s\_\mathrm{MERSI2\_24}} = -0.03 + 0.999\varepsilon_{s\_\mathrm{ASTER\_13}}$$
$$+ 0.031\varepsilon_{s\_\mathrm{ASTER\_14}} \tag{9}$$

$$\varepsilon_{s\_\mathrm{MERSI2\_25}} = -0.0155 + 0.033\varepsilon_{s\_\mathrm{ASTER\_10}}$$
$$+ 0.033\varepsilon_{s\_\mathrm{ASTER\_11}}$$
$$- 0.087\varepsilon_{s\_\mathrm{ASTER\_12}} + 0.015\varepsilon_{s\_\mathrm{ASTER\_13}}$$
$$+ 0.851\varepsilon_{s\_\mathrm{ASTER\_14}} \tag{10}$$

where $\varepsilon_{s\_\mathrm{MERSI2\_2k}}(k = 24/25)$ is the emissivity of bare soil of MERSI-2 band $k$ and $\varepsilon_{s\_\mathrm{ASTER\_k}}(k = 9\text{--}14)$ is the emissivity of bare soil of ASTER channel $k$.
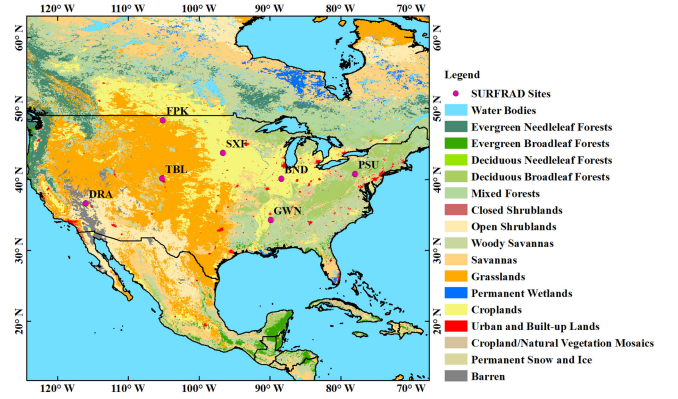


Fig. 4. Geographic locations of the SURFRAD sites (the background map is the MODIS MCD12Q1 product of 2019).

After obtaining the bare soil emissivity in each pixel of MERSI-2 TIR bands, the LSE for each MERSI-2 pixel can be calculated by (11) and (12)

$$\varepsilon_{\mathrm{MERSI2}\_i}{}' = \varepsilon_{v\_\mathrm{MERSI2}\_i}P_{v\_\mathrm{MERSI2}}$$
$$+ \varepsilon_{s\_\mathrm{MERSI2}\_i}\left(1 - P_{v\_\mathrm{MERSI2}}\right) \tag{11}$$

where $\varepsilon_{\mathrm{MERSI2}\_i}{}'$ is the vegetation adjusted MERSI-2 emissivity of band $i$, $\varepsilon_{v\_\mathrm{MERSI2}\_i}$ and $\varepsilon_{s\_\mathrm{MERSI2}\_i}$ are the emissivity of vegetation and bare soil components of MERSI-2 band $i$, respectively, and $P_{v\_\mathrm{MERSI2}}$ is the FVC calculated from the NDVI using (6). A similar calculation to adjust the snow cover using the MYD10A1 product in term of (12)

$$\varepsilon_{\mathrm{MERSI2}\_i}{}'' = \varepsilon_{s\_\mathrm{MERSI2}\_i}P_{s\_\mathrm{MERSI2}}$$
$$+ \varepsilon_{\mathrm{MERSI2}\_i}{}'\left(1 - P_{s\_\mathrm{MERSI2}}\right) \tag{12}$$

where $\varepsilon_{\mathrm{MERSI2}\_i}{}''$ is the vegetation and snow adjusted MERSI-2 emissivity of band $i$, $\varepsilon_{s\_\mathrm{MERSI2}\_i}$ is the emissivity of snow of MERSI-2 band $i$, and $P_{s\_\mathrm{MERSI2}}$ is the snow cover fraction which is obtained from MYD10A1.

### C. LST Validation Methods

In this study, two different methods were used to validate the retrieved LST of MERSI-2, namely, validation using *in situ* measurements and intercomparison using MODIS LST products. To quantify the accuracy of retrieved LST, bias and RMSE were used to as the evaluation index.

*1) LST Validation Using* In Situ *Measurements: In situ* LST comes from the surface radiation budget network (SURFRAD). The SURFRAD network was established by the National Oceanic and Atmospheric Administration in 1993 to support climate-related research over the United States by providing long-term, continuous, and accurate *in situ* surface radiation budget [75]. The system now has seven sites in different climatological regions of the United States (as shown in Fig. 4). To calculate *in situ* LST, quality-controlled measurements of broadband hemispherical upwelling and downwelling longwave radiation are provided by SURFRAD sites every 3 min (before 2009) or every minute (after 2009). Many studies have used SURFRAD measurements to validate LST retrieval from satellites [42],

[76]–[78]. In SURFRAD sites, two pyrgeometers (Eppley Precision Infrared Radiometer) mounted at 10-m height measure the downwelling and upwelling longwave radiation in the spectral range from 4.0–50.0 $\mu$m. Guillevic *et al.* [79] reported that, considering the instrumental error, less than 1-K uncertainty is observed from the site. The spatial representativeness of the pyrgeometers is approximately $70 \times 70$ m at the surface [78]. MERSI-2 TIR bands images have a spatial resolution of 250 m. Thus, the seven sites need to be validated whether they could be regarded as a uniform surface when the spatial resolution is equal to or greater than 250 m. The ASTER LST product (AST_08) is often used to evaluate the homogeneity of *in situ* sites, which has a high-spatial resolution of 90 m. Hence, a six-year period (2015–2020) of ASTER LST product was adopted to obtain the mean of stdev for each SURFRAD sites in a subset of 270 $\times$ 270 m during nighttime. Table III shows the mean stdev for the LST of SURFRAD sites, which were both lower than 0.5 K. Therefore, all sites could be regarded as homogenous. Nevertheless, Wang *et al.* [38] reported that Bondville site would have a significant contrast with the adjacent areas because of the farming in April and May every year, and the Goodwin Creek site has larger thermal inertia because of its location on a piece of grassland surrounded by broadleaf deciduous forest. Therefore, in this study, Bondville site data in April and May and Goodwin Creek site data all the year round were discarded.

The *in situ* LST was calculated using

$$\text{LST} = \left[ \frac{F^{\uparrow} - (1 - \varepsilon_{bb}) \times F^{\downarrow}}{\varepsilon_{bb} \times \sigma} \right]^{0.25} \tag{13}$$

where $F^{\uparrow}$ and $F^{\downarrow}$ are the measured surface upwelling longwave radiation and measured atmospheric downwelling longwave radiation, respectively; $\sigma$ is the Stefan Boltzmann constant $(5.67 \times 10^{-8}$ W m$^{-2}$ K$^{-4})$; and $\varepsilon_{bb}$ is the surface broadband emissivity, which was calculated using (14) according to Cheng *et al.* [80]

$$\varepsilon_{bb} = 0.197 + 0.025\varepsilon_{10} + 0.057\varepsilon_{11}$$
$$+ 0.237\varepsilon_{12} + 0.333\varepsilon_{13} + 0.146\varepsilon_{14} \tag{14}$$

where $\varepsilon_k (k = 10$–$14)$ is the mean emissivity of ASTER GEDv3 bands 10–14 in this study.

*2) LST Validation Using MODIS LST Products:* The intercomparison method is to compare the retrieved LST from a satellite with the well-validated LST from another satellite [81]–[83]. In this study, the MYD11_L2 and MYD21_L2 products were used for intercomparing which imaging time differed from the MERSI-2 data by 5 min. Before comparison, the quality pixels of the MODIS LST products were remained according to the quality control data. Then, the MERSI-2 retrieved LST were resampled to the spatial resolution of the MODIS LST products.

## IV. RESULTS

### A. Accuracy of MERSI-2 SW Algorithm

Fig. 5 shows the variation of RMSEs of the MERSI-2 SW algorithm with VZAs at each WVC subrange. The RMSE increases with the increase of WVC and VZA. The RMSE is less
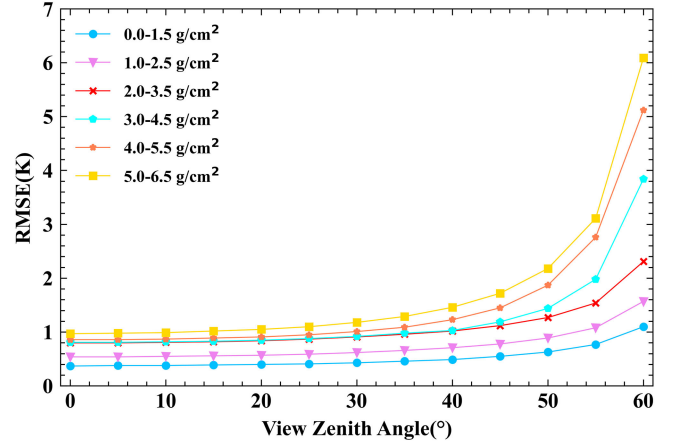


Fig. 5. RMSE of MERSI-2 SW algorithm.

than 1.5 K at each WVC subrange when VZA is less than 40° and is less than 1.5 K in all VZAs when WVC is less than 2.5 g/cm². The RMSE is greater than 3.5 K at 3–4.5 g/cm² subrange when VZA reaches 60° and is under 2 K when VZA is 55°. Therefore, in the region with a moist atmosphere, the pixels with a VZA greater than 55° were not recommended to use for retrieving LST.

### B. LST Validation Results Using In Situ *Measurements*

The MERSI-2 L1 level data in 2019 and 2020 (January, February, April, May, July, August, October, and November) correspond to winter, spring, summer, autumn, and spring over the United States, which were used to retrieve LST. All the MERSI-2 data were divided into daytime and nighttime. The number of retrieved sites LSTs are 176 and 181 at daytime and nighttime, respectively.

Although the cloud mask product and the means of visual interpretation were applied to identify clear pixels before retrieving LST, some pixels contaminated by cloud may still be remained. Furthermore, there is considerable horizontal stripe noise in MERSI-2 TIR bands images; thus, MERSI-2 retrieved LSTs that have many outliers. To obtain robust retrieved LST values, the removal strategy from Sobrino *et al.* [84] was adopted. The difference between MERSI-2 retrieved and *in situ* measurements higher than three times the theoretical algorithm RMSEs was considered outliers and was removed from the validation statistics computation. The RMSEs of MERSI-2 SW algorithm is divided into 78 values by WVC subranges and VZAs, and the VZA of MERSI-2 retrieved sites' LSTs range from 0° to 60°. Therefore, to validate comprehensively the accuracy of MERSI-2 retrieved LSTs, two theoretical algorithm RMSEs were adopted. One is the theoretical algorithm RMSE of medium VZA and medium WVC, and the other is the theoretical algorithm RMSE of maximal VZA and medium WVC. The retrieved site LSTs remained over 58% with two theoretical algorithm RMSEs. As shown in Fig. 6(a) and (b), after removing the outliers using the first theoretical algorithm RMSE, the biases between retrieved LSTs and *in situ* LSTs are –0.213 and –0.280 K at daytime and nighttime, respectively, and the
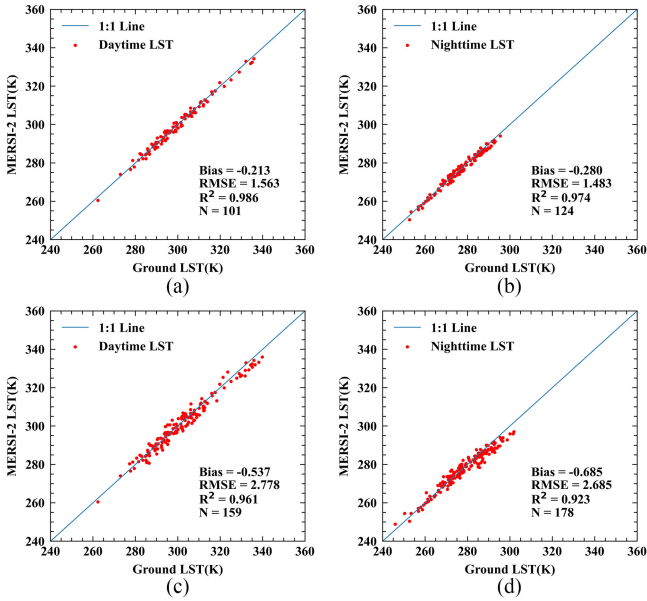
Fig. 6.   Scatterplots of the comparison between retrieved LSTs and *in situ* LSTs. (a) LSTs at daytime with the first removal strategy (theoretical algorithm RMSE is 2.745 K). (b) LSTs at nighttime with the first removal strategy. (c) LSTs during the day with the second removal strategy (theoretical algorithm RMSE is 7.252 K). (d) LSTs at nighttime with the second removal.



Fig. 7.   Detailed LST display of the study region. (a) MERSI-2. (b) MYD11_L2. (c) MYD21_L2.

RMSEs between retrieved LSTs and *in situ* LSTs are 1.563 and 1.483 K at daytime and nighttime, respectively. As shown in Fig. 6(c) and (d), after removing the outliers using the second theoretical algorithm RMSE, the bias between retrieved LSTs and *in situ* LSTs are −0.537 and −0.685 K in daytime and nighttime, respectively, and the RMSEs between retrieved LSTs and *in situ* LSTs are 2.778 and 2.685 K in daytime and nighttime, respectively. The results show that the retrieved LSTs were both highly consistent with the *in situ* LSTs, the overall retrieved LSTs is lower than ground measurements. And the RMSEs of nighttime are lower than that of daytime because the surface is not affected owing to the sunlight and shadows at night [84].

## C. LST Validation Results Using MODIS LST Products

The region of intercomparison located in the range of 36.84 °N–44.15 °N and 115.89 °E–123.01 °E, which is in the Bohai sea area of China.

Fig. 7 is the detailed LST display of the study region. As shown in Fig. 7(a)–(c), the spatial distribution of the MERSI-2 retrieved LST is consistent with MYD11 and MYD21 LST nearly, and the values of the LST is higher than the MYD11 2–3 K and MYD21 1–2 K, respectively. In addition, as shown in Fig. 7(a), the spatial distribution of the LST is unnatural in some areas because of the influence of the stripe noise in MERSI-2 TIR bands images [85].

Fig. 8(a) shows that the bias and RMSE between MERSI-2 retrieved LST and MYD11 LST are 2.885 and 3.285 K, respectively. Fig. 8(b) shows that the bias and RMSE between MERSI-2 retrieved LST and MYD21 LST are 1.492 and 2.258 K, respectively. However, a large number of LST values deviate far from the 1:1 line perhaps because of the influence of the stripe noise.
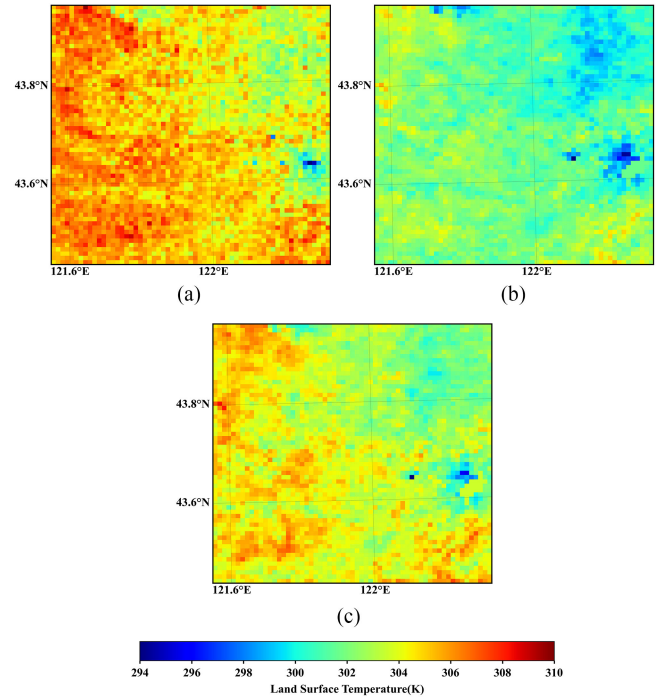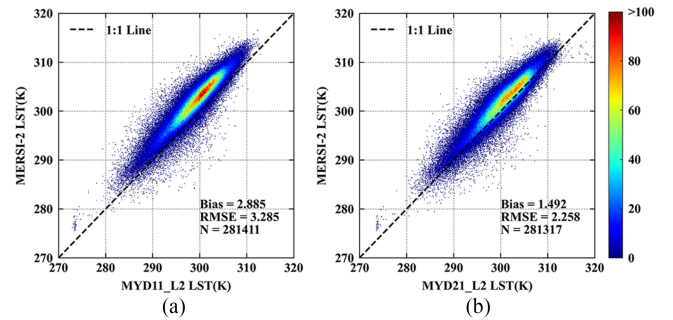


Fig. 8.   Density scatterplots of the comparison between MERSI-2 retrieved LST and MODIS LST products. (a) MERSI-2 and MYD11_L2. (b) MERSI-2 and MYD21_L2.

## V. DISCUSSIONS

### A. Sensitivity Analysis of MERSI-2 SW Algorithm

Wan *et al*. [7] noted that LSE, sensor noise, and WVC are primary uncertainties that cause errors in LST retrieval using the SW algorithm. Therefore, the sensitivity of the SW algorithm about the above three parameters was evaluated.

To evaluate the sensitivity of the SW algorithm to LSE, 1% uncertainty (about 0.01) of LSE at each TIR bands was added during LST retrieval using the SW algorithm. As shown in Fig. 9(a), the increased RMSEs tend to decrease with the increase of VZAs and the decrease of WVC. The minimum of increased RMSEs is 0.01 K when VZA is 60° and WVC is at the subranges of [4–5.5] or [5–6.5] g/cm$^2$. The maximum of increased RMSEs is 0.91 K when WVC is at the subrange of [5–6.5] g/cm$^2$ and the VZA is 0°, 5°, or 10°. The results indicated that the influence of
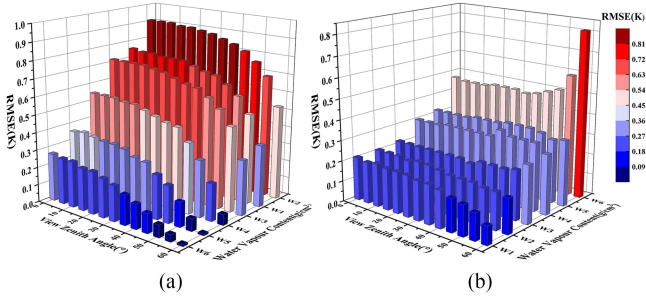
Fig. 9. Histogram of the LST RMSE caused by the uncertainty of the LSE and WVC. (a) LST RMSE caused by LSE uncertainty (about 0.001). (b) LST RMSE caused by the sensor noise (0.4 K) (W1:WVC∈[0, 1.5]; W2:WVC∈[1, 2.5]; W3:WVC∈[2, 3.5]; W4:WVC∈[3, 4.5]; W5:WVC∈[4, 5.5]; W6:WVC∈[5, 6.5]).
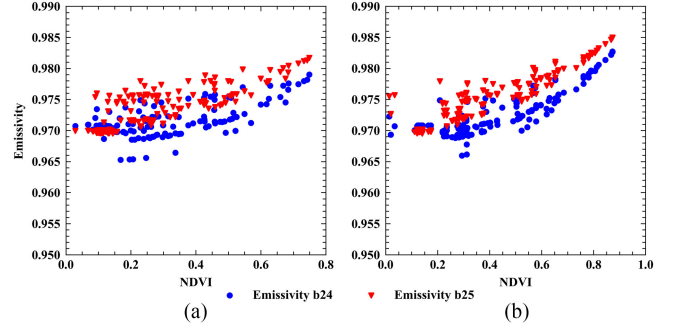


Fig. 10. Scatterplots of variation of LSE depending NDVI for SURFRAD sites. (a) Daytime. (b) Nighttime.



Fig. 11. Scatterplots of LST deviation depending WVC and VZA. (a) Daytime. (b) Nighttime.

WVC and VZA greatly exceed the LSE in the moist atmosphere when VZA is large.

The noise equivalent differential temperature (NE△T) of the TIR channels of MERSI-2 was designed as 0.4 K. To evaluate the sensitivity of the SW algorithm to sensor noise, a Gaussian-distribution noise with a stdev of 0.4 K at each TIR bands was added during LST retrieval using the SW algorithm. As shown in Fig. 9 (b), the increased RMSE in each condition is similar when the subrange of the WVC is below 5–6.5 g/cm². The minimum of the increased RMSEs is 0.09 K when VZA is 60° and WVC is at the subrange of [0–1.5] g/cm². The increased RMSEs are similar in each VZA at multiple low or medium subranges of WVC perhaps because the influence of sensor noise is small in a dry atmosphere. The maximum of increased RMSEs is 0.81 K when WVC is at the subrange of 5–6.5 g/cm² and VZA is 60°.

The WVC was divided into six subranges with an overlap of 0.5 g/cm² in this study. Each of the two adjacent subranges corresponds to different algorithm coefficients. Therefore, the influence of the uncertainty of WVC to the SW algorithm was mainly caused by using incorrect algorithm coefficients because of misclassified WVC subranges. Therefore, the RMSEs caused by using the coefficients of adjacent WVC subranges when VZA is 0° were calculated. The results in Table IV show that the misclassification of WVC led to a significant increase in LST estimation errors. The minimum of increased RMSEs is 0.26 K for the coefficients of WVC ∈ [0–1.5] g/cm² incorrectly used in the case of WVC ∈ [1–2.5] g/cm². The maximum increased RMSE was 1.46 K for the coefficients of WVC ∈ [3–4.5] g/cm² incorrectly used in case of WVC ∈ [2–3.5] g/cm². In the practical retrieval, to reduce this effect, the LST will be estimated with the algorithm coefficients of adjacent subranges, and their averaged value will be considered as the final LST [86].

### B. Analysis for the Deviation Between MERSI-2 LST and In Situ LST

To analyze reasons for the performance of our algorithm's accuracy in *in situ* validation, the scatterplots of LSE versus NDVI for SURFRAD sites were drawn, and the scatterplots of deviation versus WVC and VZA were also drawn. As shown in Fig. 10, the LSE is proportional to the increase of NDVI, which is indicated that LSE of MERSI-2 could be well estimated
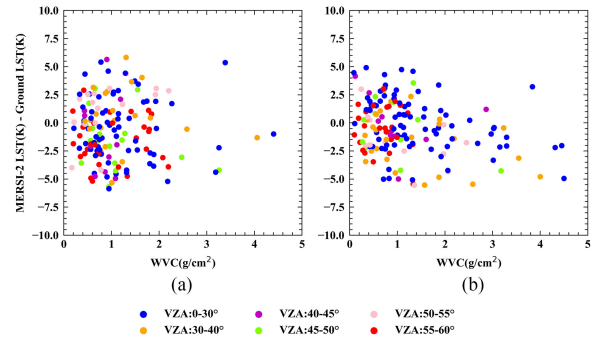
dynamically from the ASTER GED product. Zhang *et al.* [49] compared the emissivity of soil samples, which were collected from a spectrograph and derived from satellite using the ASTER GED product, respectively, and the average overestimation of those is 0.007. The overestimation of LSE will cause the significant underestimation of retrieved LST. As shown in Fig. 11, WVC of the SURFRAD sites are mostly in low and medium range because they are all in mid-latitude region. In particular, the retrieved deviation in the samples with 0–30° (blue points) exists in most situations which are greater than the samples with 55–60° (red points). In theoretical accuracy, however, the algorithm's deviation is proportional to the increase of VZA. Hence, we preliminarily infer that there exist other factors to cause this situation, such as the influence of stripe noise.

### C. Analysis of the Difference Between the MERSI-2 and MODIS LST Products

To analyze further the difference between MERSI-2 retrieved LST and MODIS LST products, the boxplots of MERSI-2 and MODIS TIR bands were drawn (as shown in Fig. 12). Two situations according to whether NDVI value is larger than 0.2 were divided. The reason is that the region can be regarded as a vegetated area when the NDVI value is larger than 0.2 [25]. As shown in Fig. 12, the LSE of the MERSI-2 and the MYD21 TIR bands are lower than that of the MYD11 TIR bands in barren and vegetated areas. Furthermore, the variation range of the LSE of MERSI-2 and MYD21 fluctuates greatly, whereas that of MYD11 is narrow because the estimation method of
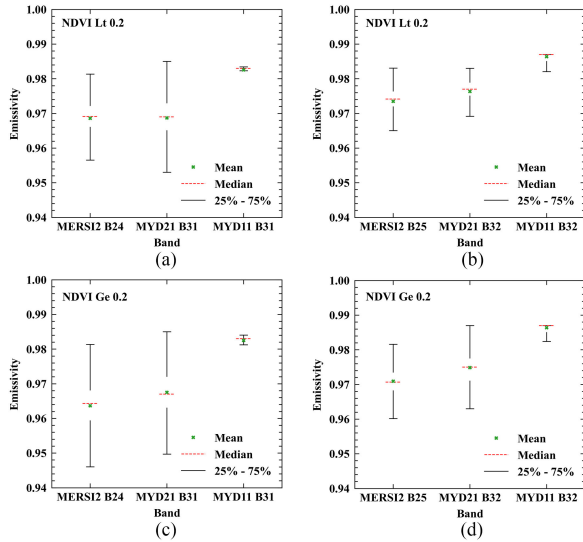
Fig. 12. Boxplots of MERSI-2 and MODIS TIR bands. (a) LSE of MERSI-2 band 24 and MYD21/MYD11 band 31 when the NDVI is less than 0.2. (b) LSE of MERSI-2 band 25 and MYD21/MYD11 band 32 when the NDVI is less than 0.2. (c) LSE of MERSI-2 band 24 and MYD21/MYD11 band 31 when the NDVI is equal or greater than 0.2. (d) LSE of MERSI-2 band 25 and MYD21/MYD11 band 32 when the NDVI is equal or greater than 0.2.

MYD11 LSE, which is a classification-based emissivity method in which only one value can be obtained on one kind of surface. The accuracy of the MODIS land classification product is 75%, which means that approximately 25% of pixels are misclassified and given inaccurate emissivity values [41]. In contrast, the real surface characteristic can be well reflected by the dynamic LSE of MERSI-2 and MYD21. In the barren area, the mean LSE of MERSI-2 band 24 is lower than that of MYD21 band 31 0.0001, and the mean LSE of MERSI-2 band 25 is lower than that of MYD21 band 32 0.003. In the vegetated area, the mean LSE of MERSI-2 band 24 is lower than that of MYD21 band 31 0.003, and the mean LSE of MERSI-2 band 25 is lower than that of MYD21 band 32 0.004.

Table V shows the relative accuracy of MERSI-2 LST and MODIS LST products in barren and vegetated areas, which indicate that the difference between the two is smaller in barren areas.

SW algorithm is sensitive to LSE, and an error of 0.005 can result in differences of LST of at least 1 K [87]. Therefore, the LST underestimation of MYD11 was mainly because of the overestimation of LSE. The LST of MERSI-2 was slightly higher than MYD21 because of the MERSI-2 LSE, which was slightly higher than MYD21 LST. Furthermore, the coefficients of the SW algorithm for retrieving MERSI-2 LST and MYD11 LST were different, which may also result in a difference between the two LST values.

## VI. CONCLUSION

An operational SW algorithm for FY-3D MERSI-2 was developed in this study. First, the simulation dataset was established by the MODTRAN 5.2 to obtain the algorithm coefficients for MERSI-2. Subsequently, in the practical retrieval, the precise

coefficients were obtained according to WVC and VZA, WVC was obtained from the ERA5 dataset, and LSE was dynamically estimated using ASTER GEDv3 and FVC. In the end, the accuracy of the algorithm in the retrieval was validated using two methods such as *in situ* validation and intercomparison.

The SW algorithm has high-overall accuracy, the RMSEs of the algorithm are between 0.37 and 6.09 K in all WVC and VZA ranges, and the RMSE is less than 1.5 K when VZA is less than 40° or WVC is less than 2.5 g/cm². The maximum increased RMSEs of the algorithm are 0.91, 0.81, and 1.46 K because of the uncertainty of LSE, sensor noise, and WVC.

In the phase of validation through using *in situ* LST, the retrieved LST was compared with *in situ* LST in 2019 and 2020 (January, February, April, May, July, August, October, and November), and the results indicated that the retrieved LST was highly consistent with the *in situ* LST. During daytime, the RMSEs (biases) of the operational SW algorithm were between 1.563 (–0.213) and 2.778 K (–0.537 K), during nighttime, the RMSEs (biases) of the operational SW algorithm were between 1.483 (–0.280) and 2.685 K (–0.685 K), reaching the accuracy of the commonly used remote sensing LST products.

In the phase of validation using MODIS LST products, the retrieved LST of MERSI-2 was compared with Collection 6 MYD11_L2 and MYD21_L2 LST products. The results indicated that MERSI-2 LST was more consistent with the MYD21 LST, and the RMSE (bias) between the two LST is 2.258 K (1.492 K). Moreover, the smaller differences between MERSI-2 LST and MODIS LST in barren areas, and the underestimation of emissivity of the two TIR bands compared with that of MYD11 and MYD21 is the main reason for the overestimation of the LST of MERSI-2.

The validation of the retrieved LST using *in situ* LST may be slightly off because of the influence of the stripe noise of MERSI-2 TIR images. Although some outliers were removed in this study, avoiding the situation which the deviation with *in situ* LSTs became smaller because the stripe noise remained is difficult. Therefore, future work should focus on removing the stripe noise of MERSI-2 TIR images to take full advantage them, and in addition to developing a LST retrieval algorithm in theory that is more applicable to MERSI-2 data and considering daytime and nighttime separately.

## REFERENCES

[1] B. Cao *et al.*, "A review of earth surface thermal radiation directionality observing and modeling: Historical development, current status and perspectives," *Remote Sens. Environ.*, vol. 232, 2019, Art. no. 111304.

[2] S.-B. Duan, Z.-L. Li, B.-H. Tang, H. Wu, and R. Tang, "Generation of a time-consistent land surface temperature product from MODIS data," *Remote Sens. Environ.*, vol. 140, pp. 339–349, 2014.

[3] Q. Weng, "Thermal infrared remote sensing for urban climate and environmental studies: Methods, applications, and trends," *ISPRS J. Photogrammetry Remote Sens.*, vol. 64, no. 4, pp. 335–344, 2009.

[4] W. Zhao, A. Li, H. Jin, Z. Zhang, J. Bian, and G. Yin, "Performance evaluation of the triangle-based empirical soil moisture relationship models based on Landsat-5 TM data and in situ measurements," *IEEE Trans. Geosci. Remote Sens.*, vol. 55, no. 5, pp. 2632–2645, May 2017.

[5] Z.-L. Li *et al.*, "Satellite-derived land surface temperature: Current status and perspectives," *Remote Sens. Environ.*, vol. 131, pp. 14–37, 2013.

[6] J. A. Sobrino, V. Caselles, and C. Coll, "Theoretical split-window algorithms for determining the actual surface temperature," *Il Nuovo Cimento C*, vol. 16, no. 3, pp. 219–236, 1993.

[7] W. Zhengming and J. Dozier, "A generalized split-window algorithm for retrieving land-surface temperature from space," *IEEE Trans. Geosci. Remote Sens.*, vol. 34, no. 4, pp. 892–905, Jul. 1996.

[8] F. Becker and Z.-L. Li, "Towards a local split window method over land surfaces," *Int. J. Remote Sens.*, vol. 11, no. 3, pp. 369–393, 2007.

[9] Z. Qin, A. Karnieli, and P. Berliner, "A mono-window algorithm for retrieving land surface temperature from Landsat TM data and its application to the Israel-Egypt border region," *Int. J. Remote Sens.*, vol. 22, no. 18, pp. 3719–3746, 2010.

[10] J. C. Jiménez-Muñoz and J. A. Sobrino, "A generalized single-channel method for retrieving land surface temperature from remote sensing data," *J. Geophysical Res., Atmospheres*, vol. 108, no. D22, 2003.

[11] C. Coll, V. Caselles, E. Valor, and R. Niclòs, "Comparison between different sources of atmospheric profiles for land surface temperature retrieval from single channel thermal infrared data," *Remote Sens. Environ.*, vol. 117, pp. 199–210, 2012.

[12] A. Gillespie, S. Rokugawa, T. Matsunaga, J. S. Cothern, S. Hook, and A. B. Kahle, "A temperature and emissivity separation algorithm for advanced spaceborne thermal emission and reflection radiometer (ASTER) images," *IEEE Trans. Geosci. Remote Sens.*, vol. 36, no. 4, pp. 1113–1126, Jul. 1998.

[13] T. Islam, G. C. Hulley, N. K. Malakar, R. G. Radocinski, P. C. Guillevic, and S. J. Hook, "A physics-based algorithm for the simultaneous retrieval of land surface temperature and emissivity from VIIRS thermal infrared data," *IEEE Trans. Geosci. Remote Sens.*, vol. 55, no. 1, pp. 563–576, Jan. 2017.

[14] S. Zhou and J. Cheng, "An improved temperature and emissivity separation algorithm for the advanced Himawari imager," *IEEE Trans. Geosci. Remote Sens.*, vol. 58, no. 10, pp. 7105–7124, Oct. 2020.

[15] B. Tang, Y. Bi, Z.-L. Li, and J. Xia, "Generalized split-window algorithm for estimate of land surface temperature from Chinese geostationary FengYun meteorological satellite (FY-2C) data," *Sensors*, vol. 8, no. 2, pp. 933–951, 2008.

[16] Y. Yu, J. L. Privette, and A. C. Pinheiro, "Evaluation of split-window land surface temperature algorithms for generating climate data records," *IEEE Trans. Geosci. Remote Sens.*, vol. 46, no. 1, pp. 179–192, Jan. 2008.

[17] Z. Wan and Z. L. Li, "Radiance-based validation of the V5 MODIS land-surface temperature product," *Int. J. Remote Sens.*, vol. 29, no. 17-18, pp. 5373–5395, 2010.

[18] J. C. Jimenez-Munoz and J. A. Sobrino, "Feasibility of retrieving land-surface temperature from ASTER TIR bands using two-channel algorithms: A case study of agricultural areas," *IEEE Geosci. Remote Sens. Lett.*, vol. 4, no. 1, pp. 60–64, Jan. 2007.

[19] C. Gao *et al.*, "Land surface temperature retrieval from FY-3C/VIRR data and its cross-validation with Terra/MODIS," *IEEE J. Sel. Topics Appl. Earth Observ. Remote Sens.*, vol. 10, no. 11, pp. 4944–4953, Nov. 2017.

[20] G.-M. Jiang, W. Zhou, and R. Liu, "Development of split-window algorithm for land surface temperature estimation from the VIRR/FY-3A measurements," *IEEE Geosci. Remote Sens. Lett.*, vol. 10, no. 4, pp. 952–956, Jul. 2013.

[21] B.-H. Tang, K. Shao, Z.-L. Li, H. Wu, F. Nerry, and G. Zhou, "Estimation and validation of land surface temperatures from Chinese second-generation polar-orbit FY-3A VIRR data," *Remote Sens.*, vol. 7, no. 3, pp. 3250–3273, 2015.

[22] C. Du, H. Ren, Q. Qin, J. Meng, and S. Zhao, "A practical split-window algorithm for estimating land surface temperature from Landsat 8 data," *Remote Sens.*, vol. 7, no. 1, pp. 647–665, 2015.

[23] J. C. Jiménez-Muñoz, J. A. Sobrino, D. Skoković, C. Mattar, and J. Cristóbal, "Land surface temperature retrieval methods from Landsat-8 thermal infrared sensor data," *IEEE Geosci. Remote Sens. Lett.*, vol. 11, no. 10, pp. 1840–1843, Oct. 2014.

[24] J. A. Sobrino, J. C. Jiménez-Muñoz, and L. Paolini, "Land surface temperature retrieval from LANDSAT TM 5," *Remote Sens. Environ.*, vol. 90, no. 4, pp. 434–440, 2004.

[25] X. Meng, J. Cheng, S. Zhao, S. Liu, and Y. Yao, "Estimating land surface temperature from Landsat-8 data using the NOAA JPSS enterprise algorithm," *Remote Sens.*, vol. 11, no. 2, 2019.

[26] Y. Yunyue, J. L. Privette, and A. C. Pinheiro, "Analysis of the NPOESS VIIRS land surface temperature algorithm using MODIS data," *IEEE Trans. Geosci. Remote Sens.*, vol. 43, no. 10, pp. 2340–2350, Oct. 2005.

[27] J. Yang, J. Zhou, F.-M. Göttsche, Z. Long, J. Ma, and R. Luo, "Investigation and validation of algorithms for estimating land surface temperature from Sentinel-3 SLSTR data," *Int. J. Appl. Earth Observation Geoinformation*, vol. 91, 2020, Art. no. 102136.

[28] Y. Chen, S.-B. Duan, H. Ren, J. Labed, and Z.-L. Li, "Algorithm development for land surface temperature retrieval: Application to Chinese Gaofen-5 data," *Remote Sens.*, vol. 9, no. 2, 2017, Art. no. 161.

[29] X. Meng and J. Cheng, "Estimating land and sea surface temperature from cross-calibrated Chinese Gaofen-5 thermal infrared data using split-window algorithm," *IEEE Geosci. Remote Sens. Lett.*, vol. 17, no. 3, pp. 509–513, Mar. 2020.

[30] B.-H. Tang, "Nonlinear split-window algorithms for estimating land and sea surface temperatures from simulated Chinese Gaofen-5 satellite data," *IEEE Trans. Geosci. Remote Sens.*, vol. 56, no. 11, pp. 6280–6289, Nov. 2018.

[31] V. Caselles, E. Valor, C. Coll, and E. Rubio, "Thermal band selection for the PRISM instrument: 1. Analysis of emissivity-temperature separation algorithms," *J. Geophysical Res., Atmospheres*, vol. 102, no. D10, pp. 11145–11164, 1997.

[32] Z.-L. Li *et al.*, "Land surface emissivity retrieval from satellite data," *Int. J. Remote Sens.*, vol. 34, no. 9/10, pp. 3084–3127, 2012.

[33] M. Wang *et al.*, "A radiance-based split-window algorithm for land surface temperature retrieval: Theory and application to MODIS data," *Int. J. Appl. Earth Observation Geoinformation*, vol. 76, pp. 204–217, 2019.

[34] W. C. Snyder, Z. Wan, Y. Zhang, and Y. Z. Feng, "Classification-based emissivity for land surface temperature measurement from space," *Int. J. Remote Sens.*, vol. 19, no. 14, pp. 2753–2774, 2010.

[35] B. H. Tang, K. Shao, Z. L. Li, H. Wu, and R. Tang, "An improved NDVI-based threshold method for estimating land surface emissivity using MODIS satellite data," *Int. J. Remote Sens.*, vol. 36, no. 19/20, pp. 4864–4878, 2015.

[36] E. Valor and V. Caselles, "Mapping land surface emissivity from NDVI: Application to European, African, and South American areas," *Remote Sens. Environ.*, vol. 57, no. 3, pp. 167–184, 1996.

[37] J. A. Sobrino, and N. Raissouni, "Toward remote sensing methods for land cover dynamic monitoring: Application to Morocco," *Int. J. Remote Sens.*, vol. 21, no. 2, pp. 353–366, 2010.

[38] H. Wang, Y. Yu, P. Yu, and Y. Liu, "Land surface emissivity product for NOAA JPSS and GOES-R missions: Methodology and evaluation," *IEEE Trans. Geosci. Remote Sens.*, vol. 58, no. 1, pp. 307–318, Jan. 2020.

[39] P. C. Guillevic *et al.*, "Validation of land surface temperature products derived from the visible infrared imaging radiometer suite (VIIRS) using ground-based and heritage satellite measurements," *Remote Sens. Environ.*, vol. 154, pp. 19–37, 2014.

[40] G. Hulley, S. Veraverbeke, and S. Hook, "Thermal-based techniques for land cover change detection using a new dynamic MODIS multi-spectral emissivity product (MOD21)," *Remote Sens. Environ.*, vol. 140, pp. 755–765, 2014.

[41] H. Li *et al.*, "Evaluation of the VIIRS and MODIS LST products in an arid area of northwest China," *Remote Sens. Environ.*, vol. 142, pp. 111–121, 2014.

[42] Y. Liu, Y. Yu, P. Yu, F. Göttsche, and I. Trigo, "Quality assessment of S-NPP VIIRS land surface temperature product," *Remote Sens.*, vol. 7, no. 9, pp. 12215–12241, 2015.

[43] G. C. Hulley, S. J. Hook, E. Abbott, N. Malakar, T. Islam, and M. Abrams, "The ASTER global emissivity dataset (ASTER GED): Mapping earth's emissivity at 100 meter spatial scale," *Geophysical Res. Lett.*, vol. 42, no. 19, pp. 7966–7976, 2015.

[44] G. C. Hulley, S. J. Hook, and A. M. Baldridge, "Validation of the North American ASTER land surface emissivity database (NAALSED) version 2.0 using pseudo-invariant sand dune sites," *Remote Sens. Environ.*, vol. 113, no. 10, pp. 2224–2233, 2009.

[45] H. Li *et al.*, "Comparison of the MuSyQ and MODIS collection 6 land surface temperature products over barren surfaces in the Heihe river basin, China," *IEEE Trans. Geosci. Remote Sens.*, vol. 57, no. 10, pp. 8081–8094, Oct. 2019.

[46] S.-B. Duan *et al.*, "Land-surface temperature retrieval from Landsat 8 single-channel thermal infrared data in combination with NCEP reanalysis data and ASTER GED product," *Int. J. Remote Sens.*, vol. 40, no. 5-6, pp. 1763–1778, 2018.

[47] J. Jiang *et al.*, "Evaluation of land surface temperature retrieval from FY-3B/VIRR data in an arid area of northwestern China," *Remote Sens.*, vol. 7, no. 6, pp. 7080–7104, 2015.

[48] R. Li *et al.*, "An operational split-window algorithm for retrieving land surface temperature from geostationary satellite data: A case study on Himawari-8 AHI data," *Remote Sens.*, vol. 12, no. 16, 2020.

[49] S. Zhang *et al.*, "Improvement of split-window algorithm for land surface temperature retrieval from Sentinel-3A SLSTR data over barren surfaces using ASTER GED product," *Remote Sens.*, vol. 11, no. 24, 2019.

[50] X. Meng, J. Cheng, and S. Liang, "Estimating land surface temperature from Feng Yun-3C/MERSI data using a new land surface emissivity scheme," *Remote Sens.*, vol. 9, no. 12, 2017.

[51] H. Wang *et al.*, "A split window algorithm for retrieving land surface temperature from FY-3D MERSI-2 data," *Remote Sens.*, vol. 11, no. 18, 2019.

[52] H. Chen, Q. Lin, Z. Wang, P. Ma, Y. Li, and A. Zhao, "Retrieval of aerosol optical depth using FY3D MERSI2 data," *J. Geo-Inf. Sci.*, vol. 22, no. 09. pp. 1887–1896, 2020.

[53] W. Wang, C. Zhang, F. Li, J. Song, P. Li, and Y. Zhang, "Extracting soil moisture from Fengyun-3D medium resolution spectral Imager-II imagery by using a deep belief network," *J. Meteorological Res.*, vol. 34, no. 4, pp. 748–759, 2020.

[54] J. Jiang *et al.*, "Land surface temperature retrieval from FY-3D MERSI-2 data in the arid/semi-arid area," *Adv. Geosciences*, vol. 09, no. 08, pp. 693–702, 2019.

[55] H. Li *et al.*, "Evaluation of atmospheric correction methods for the ASTER temperature and emissivity separation algorithm using ground observation networks in the HiWATER experiment," *IEEE Trans. Geosci. Remote Sens.*, vol. 57, no. 5, pp. 3001–3014, May 2019.

[56] A. Sekertekin and S. Bonafoni, "Land surface temperature retrieval from Landsat 5, 7, and 8 over rural areas: Assessment of different retrieval algorithms and emissivity models and toolbox implementation," *Remote Sens.*, vol. 12, no. 2, 2020.

[57] H. Li, Q. Liu, Y. Du, J. Jiang, and H. Wang, "Evaluation of the NCEP and MODIS atmospheric products for single channel land surface temperature retrieval with ground measurements: A case study of HJ-1B IRS data," *IEEE J. Sel. Topics Appl. Earth Observ. Remote Sens.*, vol. 6, no. 3, pp. 1399–1408, Jun. 2013.

[58] X. Meng and J. Cheng, "Evaluating eight global reanalysis products for atmospheric correction of thermal infrared sensor—Application to Landsat 8 TIRS10 data," *Remote Sens.*, vol. 10, no. 3, 2018.

[59] J. Yang *et al.*, "Evaluation of seven atmospheric profiles from reanalysis and satellite-derived products: Implication for single-channel land surface temperature retrieval," *Remote Sens.*, vol. 12, no. 5, 2020.

[60] H. Tonooka, "An atmospheric correction algorithm for thermal infrared multispectral data over land–A water-vapor scaling method," *IEEE Trans. Geosci. Remote Sens.*, vol. 39, no. 3, pp. 682–692, Mar. 2001.

[61] H. Tonooka, "Accurate atmospheric correction of ASTER thermal infrared imagery using the WVS method," *IEEE Trans. Geosci. Remote Sens.*, vol. 43, no. 12, pp. 2778–2792, Dec. 2005.

[62] F.-M. Göttsche and G. C. Hulley, "Validation of six satellite-retrieved land surface emissivity products over two land cover types in a hyper-arid region," *Remote Sens. Environ.*, vol. 124, pp. 149–158, 2012.

[63] S.-B. Duan *et al.*, "Validation of collection 6 MODIS land surface temperature product using in situ measurements," *Remote Sens. Environ.*, vol. 225, pp. 16–29, 2019.

[64] H. Li *et al.*, "Temperature-Based and radiance-based validation of the collection 6 MYD11 and MYD21 land surface temperature products over barren surfaces in northwestern China," *IEEE Trans. Geosci. Remote Sens.*, vol. 59, no. 2, pp. 1794–1807, Feb. 2021.

[65] R. Yao *et al.*, "A detailed comparison of MYD11 and MYD21 land surface temperature products in mainland China," *Int. J. Digit. Earth*, vol. 13, no. 12, pp. 1391–1407, 2020.

[66] M. Matricardi, F. Chevallier, G. Kelly, and J.-N. Thépaut, "An improved general fast radiative transfer model for the assimilation of radiance observations," *Quart. J. Roy. Meteorological Soc.*, vol. 130, no. 596, pp. 153–173, 2004.

[67] Z. Li, F. Petitcolin, and R. Zhang, "A physically based algorithm for land surface emissivity retrieval from combined mid-infrared and thermal infrared data," *Sci. China Ser. E: Technological Sci.*, vol. 43, no. 1, pp. 23–33, 2000.

[68] Z. Wan, "New refinements and validation of the collection-6 MODIS land-surface temperature/emissivity product," *Remote Sens. Environ.*, vol. 140, pp. 36–45, 2014.

[69] F. Chevallier, F. Chéruy, N. A. Scott, and A. Chedin, "A neural network approach for a fast and accurate computation of a longwave radiative budget," *J. Appl. Meteorol.*, vol. 37, no. 11, pp. 1385–1397, 01 Nov. 1998.

[70] F. Chevallier, A. Chédin, F. Cheruy, and J. J. Morcrette, "TIGR-like atmospheric-profile databases for accurate radiative-flux computation," *Quart. J. Roy. Meteorological Soc.*, vol. 126, no. 563, pp. 777–785, 2000.

[71] C. Coll *et al.*, "Ground measurements for the validation of land surface temperatures derived from AATSR and MODIS data," *Remote Sens. Environ.*, vol. 97, no. 3, pp. 288–300, 2005.

[72] A. M. Baldridge, S. J. Hook, C. I. Grove, and G. Rivera, "The ASTER spectral library version 2.0," *Remote Sens. Environ.*, vol. 113, no. 4, pp. 711–715, 2009.

[73] J. A. Sobrino *et al.*, "Land surface emissivity retrieval from different VNIR and TIR sensors," *IEEE Trans. Geosci. Remote Sens.*, vol. 46, no. 2, pp. 316–327, Feb. 2008.

[74] C. Wang, S.-B. Duan, X. Zhang, H. Wu, M.-F. Gao, and P. Leng, "An alternative split-window algorithm for retrieving land surface temperature from visible infrared imaging radiometer suite data," *Int. J. Remote Sens.*, vol. 40, no. 5/6, pp. 1640–1654, 2019.

[75] A. Sekertekin and S. Bonafoni, "Sensitivity analysis and validation of daytime and nighttime land surface temperature retrievals from Landsat 8 using different algorithms and emissivity models," *Remote Sens.*, vol. 12, no. 17, 2020.

[76] D. J. Ghent, G. K. Corlett, F. M. Göttsche, and J. J. Remedios, "Global land surface temperature from the along-track scanning radiometers," *J. Geophysical Res., Atmospheres*, vol. 122, no. 22, pp. 12 167–12 193, 2017.

[77] S. Li, Y. Yu, D. Sun, D. Tarpley, X. Zhan, and L. Chiu, "Evaluation of 10 year AQUA/MODIS land surface temperature with SURFRAD observations," *Int. J. Remote Sens.*, vol. 35, no. 3, pp. 830–856, 2014.

[78] K. Wang, and S. Liang, "Evaluation of ASTER and MODIS land surface temperature and emissivity products using long-term surface longwave radiation observations at SURFRAD sites," *Remote Sens. Environ.*, vol. 113, no. 7, pp. 1556–1565, 2009.

[79] P. C. Guillevic *et al.*, "Land surface temperature product validation using NOAA's surface climate observation networks—Scaling methodology for the visible infrared imager radiometer suite (VIIRS)," *Remote Sens. Environ.*, vol. 124, pp. 282–298, 2012.

[80] C. Jie, L. Shunlin, Y. Yunjun, and Z. Xiaotong, "Estimating the optimal broadband emissivity spectral range for calculating surface longwave net radiation," *IEEE Geosci. Remote Sens. Lett.*, vol. 10, no. 2, pp. 401–405, Mar. 2013.

[81] C. Gao *et al.*, "Evaluation of land surface temperature by comparing FY-3C/VIRR with Terra/MODIS and MSG/SEVIRI data," *Int. J. Remote Sens.*, vol. 40, no. 5-6, pp. 1779–1792, 2018.

[82] Y.-G. Qian, Z.-L. Li, and F. Nerry, "Evaluation of land surface temperature and emissivities retrieved from MSG/SEVIRI data with MODIS land surface temperature and emissivity products," *Int. J. Remote Sens.*, vol. 34, no. 9/10, pp. 3140–3152, 2012.

[83] I. F. Trigo, I. T. Monteiro, F. Olesen, and E. Kabsch, "An assessment of remotely sensed land surface temperature," *J. Geophysical Res.*, vol. 113, no. D17, 2008, doi: 10.1029/2008JD010035.

[84] J. A. Sobrino *et al.*, "Synergistic use of MERIS and AATSR as a proxy for estimating land surface temperature from Sentinel-3 data," *Remote Sens. Environ.*, vol. 179, pp. 149–161, 2016.

[85] K. Tang, H. Zhu, Y. Cheng, and L. Zhang, "Destriping and evaluating FY-3D MERSI-2 data with the moment matching method based on synchronous reference image," *J. Appl. Remote Sens.*, vol. 14, no. 04, 2020, Art. no. 046517.

[86] X. Ye, H. Ren, R. Liu, Q. Qin, Y. Liu, and J. Dong, "Land surface temperature estimate from Chinese Gaofen-5 satellite data using split-window algorithm," *IEEE Trans. Geosci. Remote Sens.*, vol. 55, no. 10, pp. 5877–5888, Oct. 2017.

[87] S. C. Freitas, I. F. Trigo, J. M. Bioucas-Dias, and F. M. Gottsche, "Quantifying the uncertainty of land surface temperature retrievals from SEVIRI/Meteosat," *IEEE Trans. Geosci. Remote Sens.*, vol. 48, no. 1, pp. 523–534, Jan. 2010.

**Kai Tang** received the B.Eng. degree in remote sensing science and technology from the Shandong Agricultural University, Taian, China, in 2019. He is currently working toward the M.Sc. degree in surveying engineering with the Shandong University of Science and Technology, Qingdao, China.

His research interests include the processing and analysis of remote sensing image, and the retrieval and validation of land surface temperature/emissivity.

**Ruibo Li** received the B.Eng. degree in remote sensing science and technology from the Shandong University of Science and Technology, Qingdao, China, in 2015. She is currently working toward the Ph.D. degree in photogrammetry and remote sensing with the College of Geodesy and Geomatics with Shandong University of Science and Technology, Qingdao, China, and the joint Ph.D. degree with the Aerospace Information Research Institute, Chinese Academy of Science, Beijing, China.

Her research interests include the retrieval and validation of land surface temperature/emissivity and aerosol optical depth (AOD) from satellite data.

**Hongchun Zhun** received the B.S. degree in geographical science from the Shandong Normal University, Jinan, China, in 2000, and the M.Sc. degree in cartography and geographic information system and the Ph.D. degree in photogrammetry and remote sensing from North-western University, Xian, China, in 2003 and 2008, respectively.

He is currently a Professor with the School of Surveying and Mapping, Shandong University of Science and Technology, Qingdao, China. His research interests include GIS applications, remote sensing image processing and analysis, digital elevation models and digital terrain analysis, and other aspects of teaching and research work.

**Cheng Fan** received the B.S. degree in surveying engineering from the China University of Mining and Technology, Beijing, China, in 2015. She is currently working toward the M.S. and Ph.D. degrees in cartography and geographic information system with Aerospace Information Research Institute, Chinese Academy of Science (AIR-CAS).

She has been a visiting Ph.D. student with the Netherlands Institute for Space Research (SRON) for one year working on aerosol retrieval over ocean with polarimetric measurements.

**Ping Ni** received the B.Eng. degree in remote sensing science and technology from the Shandong Agricultural University, Taian, China, in 2019. She is currently working toward the M.Sc. degree in surveying engineering with the Shandong University of Science and Technology, Qingdao, China.

Her research interests include the processing and analysis of remote sensing image, and the retrieval and validation of land surface temperature/emissivity.